

Integrated Nanogap Platform for Sub-Volt Dielectrophoretic Trapping and Real-Time Raman Imaging of Biological Nanoparticles

Christopher T. Ertsgaard,[†] Nathan J. Wittenberg,^{†,§} Daniel J. Klemme,[†] Avijit Barik,^{†,‡} Wei-Chuan Shih,^{||} and Sang-Hyun Oh^{*,†,‡,§}

[†]Department of Electrical and Computer Engineering and [‡]Department of Biomedical Engineering, University of Minnesota, Minneapolis, Minnesota 55455, United States

[§]Department of Chemistry, Lehigh University, Bethlehem, Pennsylvania 18015, United States

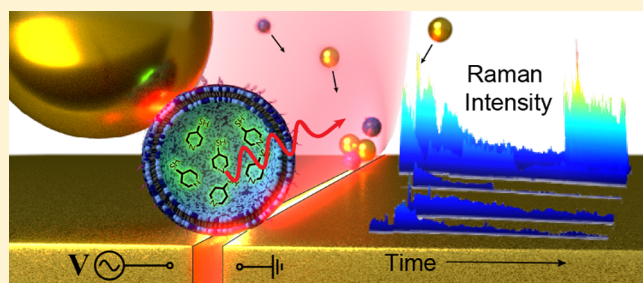
^{||}Department of Electrical and Computer Engineering, University of Houston, Houston, Texas 77204, United States

S Supporting Information

ABSTRACT: A rapid, label-free, and broadly applicable chemical analysis platform for nanovesicles and subcellular components is highly desirable for diagnostic assays. We demonstrate an integrated nanogap plasmonic sensing platform that combines subvolt dielectrophoresis (DEP) trapping, gold nanoparticles (AuNPs), and a lineated illumination scheme for real-time, surface-enhanced Raman spectroscopy (SERS) imaging of biological nanoparticles. Our system is capable of isolating suspended sub-100 nm vesicles and imaging the Raman spectra of their cargo within seconds, 100 times faster than conventional point-scan Raman systems.

Bare AuNPs are spiked into solution and simultaneously trapped with the nanovesicles along the gap to boost local optical fields. In addition, our platform offers simultaneous and delay-free spatial and temporal multiplexing functionality. These nanogap devices can be mass-produced via atomic layer lithography and provide a practical platform for high-speed SERS analysis of biological nanoparticles.

KEYWORDS: Dielectrophoresis, nanogap, Raman, surface-enhanced Raman scattering (SERS), gold nanoparticle, vesicle



Nanogap structures in metals can sustain tightly confined and boosted electromagnetic fields and they have shown promising capabilities for biosensing and particle manipulation. Applications of these structures has included: surface-enhanced Raman scattering (SERS),^{1–4} infrared absorption spectroscopy,^{5–7} optical trapping,^{8–10} and electrokinetic trapping.¹¹ By integration of some of these functions into a single platform, it is possible to build powerful instruments that can rapidly concentrate rare analytes in solution and perform sensitive spectroscopic analysis. Here we combine top-down fabrication of electrically addressable nanogap electrodes with colloidal gold nanoparticles and perform rapid, sensitive, and parallel SERS detection of biological analytes. Specifically, biological applications can benefit from our high-speed Raman imaging platform to capture and detect rare biological nanoparticles and nanovesicles.

Membrane-bound biological nanoparticles such as liposomes, cell-derived vesicles, and extracellular vesicles (EVs), are of particular interest due to their capability to compartmentalize and transport molecules in biological systems.¹² The isolation, detection, and characterization techniques for membrane-bound nanoparticles like EVs are under intense investigation.¹³ When EVs (i.e., exosomes, ~50–100 nm in diameter) are excreted naturally from cells, their

size, membrane composition, and intracellular cargo reveal important information regarding the state of their host cell.¹⁴ These features have been exploited as biomarkers in “liquid biopsies” for cancerous activity and pathological signaling,¹⁵ contributing a significant motivation for techniques that offer both rapid isolation and *in situ* multicomponent content analysis.

Since vesicles diffuse more slowly than biomolecules, it is important to speed up their delivery to the sensing surface. To overcome the diffusion limit and enable rapid analysis of biological particles, many groups have demonstrated innovative schemes including electrokinetics,¹⁶ nanofluidics,^{17–19} evaporation-driven concentration,²⁰ and microbubbles.²¹ As another promising option, dielectrophoresis (DEP)²² offers rapid concentration and isolation of nanoparticulate matter that does not depend on specific chemical binding or alterations. The DEP process commonly utilizes two electrodes in solution that are subjected to an alternating electric field (E-field). This E-field induces local dipoles within the particles that results in a net force toward or away from the E-field gradient depending

Received: June 29, 2018

Revised: July 26, 2018

Published: August 2, 2018

on the frequency of oscillation and the dielectric permittivity of the particle and surrounding medium. Due to its simplicity and scalability, DEP has been widely used to trap and manipulate cells,^{23,24} vesicles,^{25,26} and biomolecules.^{27–29}

The rapid and label-free DEP concentration scheme can be naturally coupled with and fully exploited by label-free Raman spectroscopy to analyze the trapped particles. Since Raman scattering signals from biological analytes are generally weak—even with DEP concentration - it is desirable to further boost the Raman signals via on-chip SERS detection. SERS has the capability to capture dynamic chemical changes,^{30,31} is label-free, and has a narrow bandwidth emission.³² All SERS measurements are contingent upon interactions of the analyte with a metallic substrate surface (or metallic nanoparticle).^{33,34} One simple SERS platform for membrane-bound particles exploits gold nanoparticles (AuNPs), in which the nanovesicles become “sandwiched” between other AuNPs and/or a metallic substrate. Their junction provides the necessary surface enhancement for SERS.³⁵ Chemical tagging techniques with ligand and receptor binding have been used to generate the described configuration. However, such processes require overnight incubation and hours of wet chemistry—effectively negating the rapid, label-free advantages SERS can offer. By utilizing a DEP nanogap electrode in solution to force AuNP and liposome interactions, rapid on-chip SERS analysis can be performed without chemical tags or substrate tuning.

Here we demonstrate a combined DEP and SERS platform—trapping, Raman, and imaging line (TRAIL)—that can rapidly position nanovesicles within seconds along a line and measure real-time SERS spectra from their cargo. We use a high-aspect ratio, 11 nm line-gap electrode for DEP,¹¹ which can create ultrastrong field gradients at a fraction of the voltage required by conventional microelectrodes. The SERS TRAIL is excited along the gap using a laser-line illumination to chemically image the Raman spectra 100 times faster than a similar scanning-spot Raman system.³⁶ This seamless integration of rapid DEP line-trapping and high-speed line Raman spectroscopy technique enables delay-free SERS imaging experiments for sub-100 nm vesicles, which could be capable of distinguishing vesicles, such as synthetic liposomes or EVs, by size and composition.

A common concern regarding DEP is the adverse effects large trapping voltages can have to the sample solution and its analytes. In order to overcome the thermal motion of sub-100 nm particles, conventional DEP electrodes with micrometer-scale gaps typically require a minimum trapping voltage of 10 V_{pp}.¹¹ Such large trapping voltages can cause Joule heating, bubble formation, and unfavorable electrochemical reactions.³⁷ However, DEP is a scalable technique, and by reducing the width between the electrode gaps, the DEP trapping force can be increased without raising the trapping voltage. The time averaged DEP force of a spherical particle with radius R and in a solution with a dielectric permittivity of ϵ_m is provided below.

$$F_{\text{DEP}}(\omega) = \pi \epsilon_m R^3 \operatorname{Re}(f_{\text{CM}}(\omega)) \nabla |E|^2$$

The real part of the Clausius–Mossotti factor (CMF), $\operatorname{Re}(f_{\text{CM}}(\omega))$, determines the direction of the DEP force based on the dielectric permittivity of the solution and particle. The gradient of the E -field in solution squared, $\nabla |E|^2$, correlates with the supply voltage applied across the DEP electrodes. By reducing the width between DEP electrodes, the gradient of the E -field can be increased substantially. Many groups have

explored schemes to produce nanometer-scale gaps in gold films.^{2,38,39} Previously, our group developed a 0.8 mm long and 9 nm wide gold electrode gap capable of trapping sub-100 nm dielectric particles with less than 1 V amplitude, which significantly reduces Joule heating and electrolysis while still probing a vastly large region.¹¹ The nominal electrode gap width used in the lineated DEP substrate presented here was 11 nm and the length of the active trapping region can be arbitrarily long (only limited by the wafer size) due to the unique high-throughput nature of the atomic layer lithography scheme (Figure 1a).

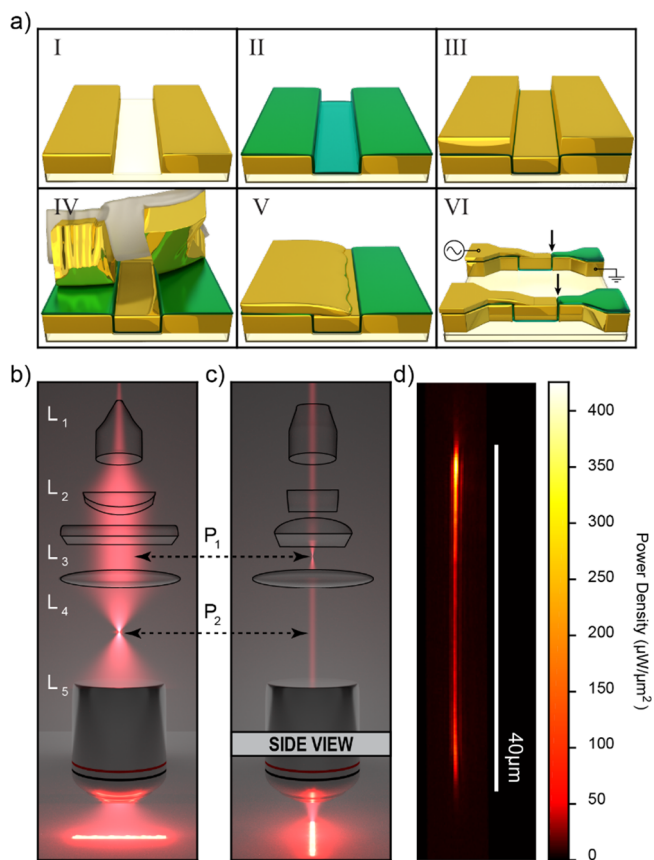


Figure 1. Nanogap-based high-speed Raman lineation imaging platform. Diagram (a) demonstrates the fabrication steps for our high-aspect-ratio lineated DEP substrate. Step 1: The first edge of the gold electrode is defined via photolithography. Step 2: A nominal 11 nm Al₂O₃ film is deposited using ALD to precisely define the width of the DEP gap. Step 3: A nonconformal evaporated layer of gold fills the trench and forms the second electrode edge. Step 4: Adhesive tape is used to peel off the excess layer of gold not filling the trench. Step 5: Gold is sputtered on one side of the trench to make electrical connection to the second electrode edge. Step 6: A final photolithography step defines the individual DEP trap sites and electrode pads for multiplexing experiments. Particles are trapped at the regions indicated by arrows. (b) Basic lens configuration of the laser-line optics using a Powell lens (L_1) and two orthogonal cylindrical lenses (L_2, L_3). The image of the laser-line is formed at P_1 and its Fourier transform is taken by a spherical lens (L_4) at P_2 before being imaged again on the sample by the microscope objective (L_5). (c) An orthogonal view of the lens configuration to highlight the “short” dimension laser-line path. (d) A power density image of the laser-line on gold through a 100× objective (NA 1.25). The max power density was measured to be 425.6 $\mu\text{W}/\mu\text{m}^2$.

Previously, line-scan Raman imaging has shown promising potential for high-speed 2D Raman imaging.^{36,40,41} On the other hand, our DEP line trap geometry does not require scanning and is ideal for integration with high-speed line imaging optics, which can efficiently distribute the available laser power along the active nanogap trapping region. Our lineation optics consisted of a Powell lens and two orthogonally rotated cylindrical lens (Figure 1b,c). Under experimental conditions, this line was focused using a 100 \times objective (NA 1.25) and aligned to the DEP gap. The image of the line was measured to be 40 μm long and 800 nm wide, which defined the length of the active region and the resolution of the imaging setup, respectively (Figure 1d). It was demonstrated that laser power greater than 1 $\text{mW}/\mu\text{m}^2$ can induce rupturing and leaking of liposome cargo.³⁵ The maximum power density along the entire length of the laser-line was measured to be 425.6 $\mu\text{W}/\mu\text{m}^2$ at the far edge of the line (Figure 1d), which is ~ 2.3 times below the reported damage threshold.

Initial experiments were performed to characterize the integrated TRAIL sensing platform using 70 nm AuNPs coated with 4-mercaptopyridine (4-MPY). This included measuring the minimum trapping voltage and reference SERS spectrum from 4-MPY (Figure 2). In all of the subsequent plots, the same maximum peak of 4-MPY, corresponding to the ring breathing/C–S mode,⁴² was plotted. Throughout all experiments slight shifts of less than 10 cm^{-1} were observed in the prominent peak positions. These are attributable to slight shifts/misalignments of the grating (less than 1 nm) and/or due to the rapidly changing local SERS environment, affecting the vibrational coupling conditions. These include continually varying interactions with the number of neighboring AuNPs during trapping, interactions with the Au mirror electrodes and the rough Au edges of the gap, all averaged together into one spectrum. Similar shifts in the SERS spectrum were observed by Hu et al. of 4-MPY excited using an Ag mirror SERS substrate, Ag foil, and Ag colloids.⁴² A complete list of the observed peaks, their bond assignments, reproducibility and statistics are including in the Supporting Information (Table S1). An imaging spectrometer was used to perform 1D imaging⁴³ along the length of the nanogap and spatially resolve SERS spectra from the AuNPs. A minimum trapping voltage was observed at 400 mV with consistent trapping at an 800 mV peak-amplitude AC signal (Figure 2a). The spatial resolution was 800 nm with an exposure time of 0.5 s per frame. A standard spot-scan Raman imaging system with the same resolution and exposure time would take 100 times longer per frame. In addition, a scan-based imaging platform inherently induces time-delays between the acquisition of pixels. If this delay is on the same time-scale as the system's dynamics or greater, these temporal artifacts become problematic, especially when performing multiplexed experiments for direct comparison. Ideally, a delay-free SERS imaging platform between pixel acquisition is desirable.

To demonstrate the advantage of delay-free pixel acquisition in capturing dynamics, a parallel DEP trap design was used with the same lineation optics and 4-MPY coated AuNPs (Figure 3). Independent traps were fabricated 10 μm in length and spaced by 10 μm (Figure 3a). A one second exposure time was used to reduce the spectral noise for a systematic comparison between parallel traps. When keeping the trapping potential near its minimum (i.e., 700 mV), consistent trap and release of the AuNPs was observed within seconds of toggling

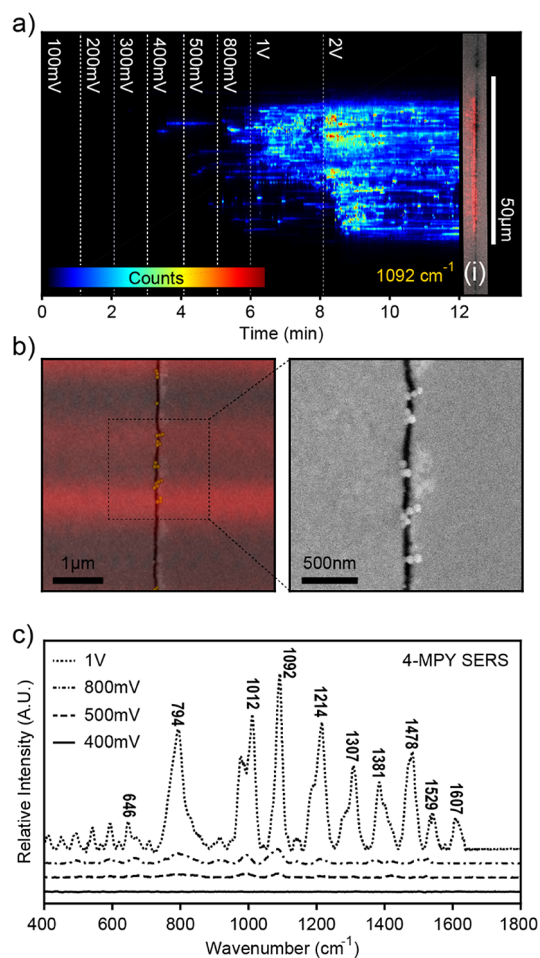


Figure 2. Minimum trapping voltage and SERS TRAIL imaging of 4-MPY-coated AuNPs. (a) Space-time plot of the trapping events as they occur in space (y-axis, 800 nm resolution) and time (x-axis, 0.5 s frames) as indicated by the intensity of the 1092 cm^{-1} SERS peak of 4-MPY coated on 70 nm AuNPs. At each dashed division, the voltage trapping amplitude of the AC signal (1 MHz) was set to the specified value. A minimum trapping voltage of 400 mV is observed with more consistent trapping at 800 mV amplitude. (i) Bright-field image of the DEP gap and laser-line spatially aligned to the space-time plot. (b) An SEM of AuNPs trapped along the gap. Due to the inherent rounded edges of the two DEP electrodes from fabrication, the gap width appears artificially larger than the nominal 11 nm width defined by the ALD film. Regions where SERS spectra were observed after the solution was dried are overlaid in red using micrometer sized alignment markers (not shown) on the left image, and the trapped AuNPs are labeled with a yellow dot. The right image demonstrates a zoomed-in SEM of the boxed region of the left SEM. It was observed that clumps with three or more AuNPs exhibit a measurable SERS signal. (c) The SERS spectra averaged across the entire 40 μm length for 10 s after the corresponding DEP supply voltages were applied and SERS background removed.

the supply voltage on and off for each trap (Figure 3b). Due to the AuNPs being weakly held at their threshold trapping voltage, larger fluctuations in the SERS intensity were observed as compared to experiments operating at a higher trapping voltage. This likely allows the AuNPs to more freely “wiggle” about and cause larger fluctuations in the SERS enhancement factor (Figure 3c). Due to the fast line illumination scheme, there is no delay between observed events on both the top and bottom device. Both are excited and collected simultaneously and the dynamics are observed across the entire SERS

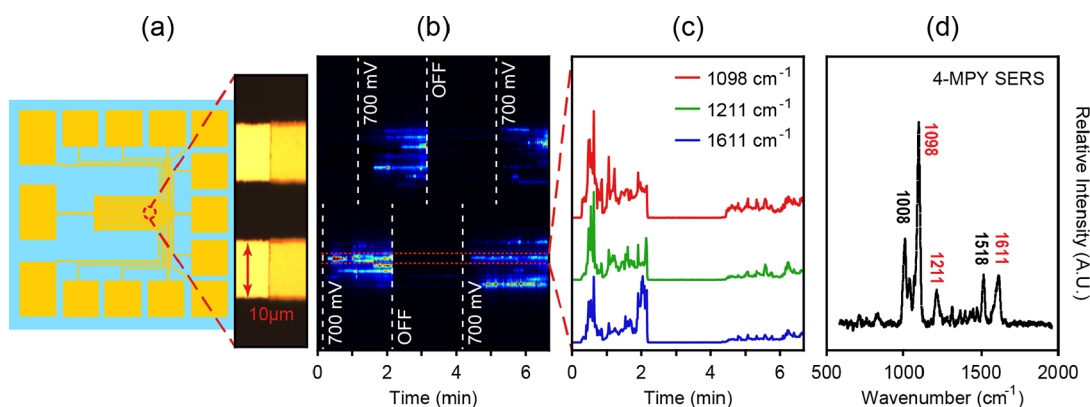


Figure 3. Delay-free spatial and temporal multiplexing functionality. (a) A schematic of our DEP substrate with 13 spatially multiplexed, parallel $10\ \mu\text{m}$ long devices. The right inset shows a microscope image of two devices used before trapping. The $11\ \text{nm}$ gap is located at the junction between the lighter and darker yellow regions. The darker yellow regions to the right of the gap is the Al_2O_3 layer. (b) A space-time plot of the trapping events of AuNPs coated with 4-MPY, as indicated by the intensity of the $1098\ \text{cm}^{-1}$ SERS peak. Trapping events are modulated in space and time across two parallel devices. An AC signal of $1\ \text{MHz}$ with $700\ \text{mV}$ amplitude is applied across the specified device at the regions indicated with a “ $700\ \text{mV}$ ” white dashed line. At the “OFF” white dashed line regions, the specified device is grounded with zero applied voltage to allow the AuNPs to diffuse away. Both devices are controlled independently and excited in parallel using our lineation optics. (c) A time-trajectory of three different 4-MPY peaks from the red-dashed region in Figure 3b. The on-off phenomenon is observed across the whole SERS spectrum. The reduction in SERS intensity upon retrapping is likely due to the number of trapped particles that returned to the same $2\ \mu\text{m}$ red-dashed region happened to be less than were originally trapped when the experiment was initiated. (d) The averaged, full SERS spectra from the red-dashed region of part b after the SERS background is removed.

spectrum (Figure 3c). This temporal information regarding trap events would be lost using a similar spot-scan system. Upon using the same imaging parameters (i.e., resolution and exposure time), there would be over a minute delay between spectra collected from the top and bottom of the two $10\ \mu\text{m}$ devices.

The same $10\ \mu\text{m}$ multiplexed DEP device was then used to measure the SERS TRAILs from 4-MPY encapsulated in nominal $50\ \text{nm}$ diameter liposomes, with an averaged measured diameter of $69.9\ \text{nm}$ using a dynamic light scattering volume distribution. Liposomes were comprised of 1,2-dimyristoyl-*sn*-glycero-3-phosphocholine (DMPC) and cholesterol (4:1 molar ratio, Avanti Polar Lipids) and are expected to remain intact upon interaction with both Au and Al_2O_3 substrates,⁴⁴ which compose our TRAIL platform. The liposome solution was then spiked with bare AuNPs to be simultaneously trapped along the gap in a random configuration. Liposomes trapped in-between the AuNPs experience an enhanced electric-field capable for SERS excitation. COMSOL simulations were made to predict the theoretical combined enhancement factor from the gap and AuNP aggregates surrounding the liposomes. A $70\ \text{nm}$ liposome, when placed along the gap and surrounded on three sides by AuNPs, experiences an average E-field enhancement factor of 3.7 inside the nanovesicle with a maximum enhancement factor of 8.3 located near the liposome membrane (Figure 4a). This equates to an average Raman intensity enhancement of 187 across the liposome and a maximum Raman intensity enhancement of 4746 near the membrane (Figure 4a). Due to this observation, it is hypothesized the SERS imaging in the TRAIL platform is most sensitive to membrane-associated components. A further study of multiple possible configurations of the AuNPs are included in the Supporting Information (Figure S1).

The DEP trapping forces exerted on a solid metallic colloid and an aqueous lipid shell are inherently different and result in different trapping volumes. The radial distance from the gap in which the DEP force exceeds that of a 1D thermal force

exerted on a sphere experiencing Brownian motion defines the trapping radius (Figure 4b). This radius, which further defines a hemicylindrical trapping volume, can be solved for using the DEP force equation provided above and numerically simulating the ∇E^2 fringe field generated by an $11\ \text{nm}$ wide gap electrode at a given DC bias. The resulting differences in trapping radius will depend on the size of each type of particle and the dielectric permittivity of the particles, which is incorporated in the CMF. The AuNPs have a CMF factor of 1 over the entire frequency range of interest ($1\ \text{Hz}$ – $10\ \text{MHz}$) (Figure 4c). However, using a simple shell model for the $70\ \text{nm}$ liposomes, assuming the permittivity and conductivity of the inner and outer medium to be the same, suggests a negative CMF factor over all frequencies of interest. This would result in a repelling DEP force rather than trapping. Zwitterionic liposomes such as DMPC can exhibit an effectively larger conductivity of the inner-medium and dielectric permittivity of the membrane than predicted.⁴⁵ This is due to an apparent surface charge accumulation of counterions to the liposome surface. Due to the similarities in structure of DMPC and DPPC, the effective conductivity and permittivity values measured by Biasio et al. for the DPPC membrane and inner-medium were used and resulted in a positive CMF value of 0.2 around $1\ \text{MHz}$ (Figure 4c). By calculating the corresponding trapping radius as an estimated upper bound, the trapping volume for the $70\ \text{nm}$ AuNPs is ~ 3 times larger than that of the $70\ \text{nm}$ liposomes (Figure 4b).

Using the same multiplexed substrate and imaging parameters as Figure 3, 4-MPY SERS was observed from the liposomes using bare AuNPs spiked in solution for surface-enhancement and there was good agreement in the peak positions for 4-MPY encapsulated in liposomes as compared to 4-MPY coated on the surface of AuNPs (Figure 5a). A minimum trapping amplitude of $600\ \text{mV}$ was measured for the $70\ \text{nm}$ liposomes with consistent trapping near $1\ \text{V}$. Negative control experiments with liposomes and no AuNPs reveal that without surface-enhancement, the Raman signal from the trapped liposomes is below the noise threshold and thus a

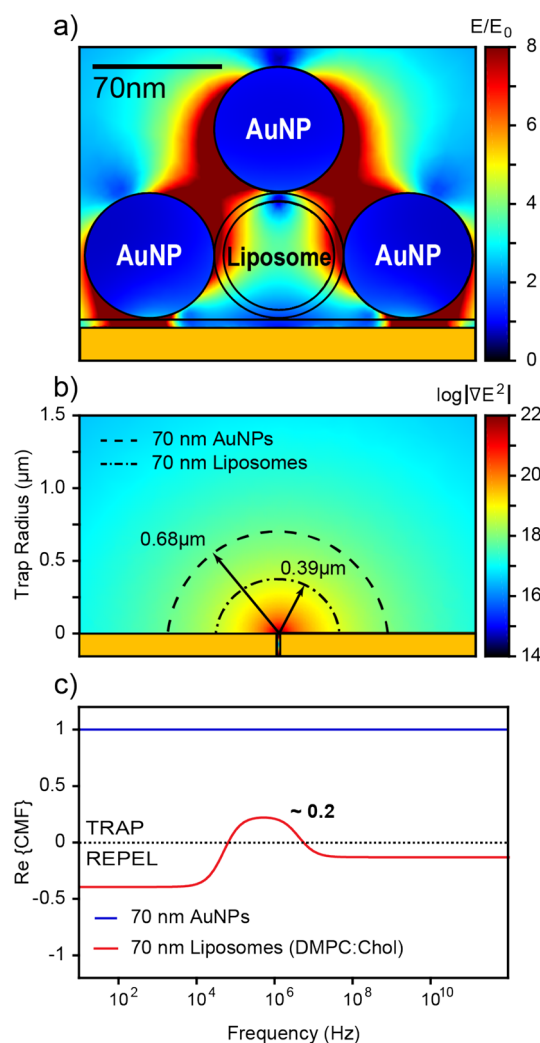


Figure 4. Simulation results for SERS enhancement, the DEP trapping volume, and CMF. (a) Cross-section parallel to the nanogap electrode demonstrating the E-field enhancement factor generated within a 70 nm liposome when surrounded on three sides by 70 nm AuNPs and an 11 nm gap electrode below. This configuration was chosen to simulate how the particles may align along the gap during trapping. (b) The theoretical trapping volume for 70 nm liposomes and 70 nm AuNPs on top of a log-scale of the ∇E^2 for an 11 nm gap electrode with 1 V DC applied. The trapping radius for the AuNPs extends ~ 1.7 times farther than that of the liposomes. (c) The real part of the CMF for 70 nm AuNPs and 70 nm zwitterionic liposomes. The 70 nm liposomes only experience trapping toward the gap when the AC frequency is around 1 MHz as compared to 70 nm AuNPs which are trapped over all frequencies of interest.

measured enhancement factor is not achievable. Occasionally, some sporadic SERS signal was detected and attributed to rough edges along the nanogap but appear randomly and sparsely between devices as observed from three control experiments, see [Supporting Information](#) (Figure S2). These negative control experiments suggest the bulk of the SERS enhancement is derived from the AuNP interactions which is consistent with the simulation results. Furthermore, the SERS signal observed confirms the main prominent peaks do originate from the liposomes encapsulating 4-MPY and not from the citrate capping agent of the AuNPs or other possible molecular contaminants whose SERS could also be excited by the AuNPs (Table S1).

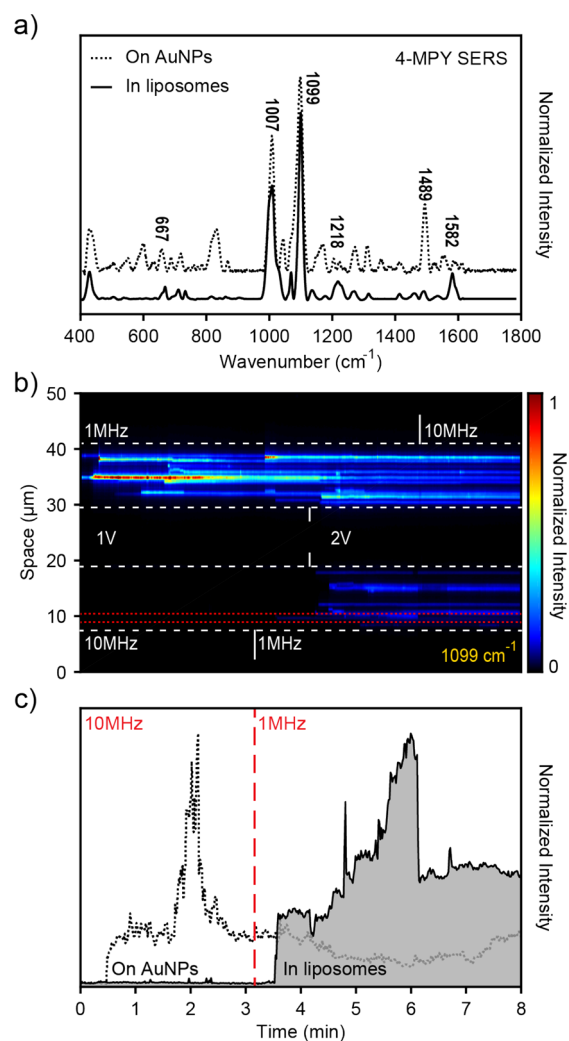


Figure 5. SERS TRAIL derived from liposome cargo as compared to coated AuNPs. (a) SERS spectra measured from the 4-MPY encapsulated liposomes spiked with bare AuNPs as compared with 4-MPY coated on AuNPs. (b) A space-time SERS TRAIL plot of trapping events indicated by the $1099\ \text{cm}^{-1}$ peak of 4-MPY encapsulated in liposomes spiked with bare AuNPs. Two $10\ \mu\text{m}$ traps are controlled independently and excited/imaged in parallel using our lineation optics. The frequency response on the SERS signal is observed, indicating the origin of the SERS signal is derived from encapsulated 4-MPY rather than AuNP bound 4-MPY. (c) Time-trajectory of the $1099\ \text{cm}^{-1}$ peak summarizing the frequency response in SERS between the encapsulated in liposomes (from the red boxed region of part b) as compared to 4-MPY coated on AuNPs. SERS from the AuNPs is seen during both 10 and 1 MHz operation whereas SERS from the liposomes occurs only after the device is switched to 1 MHz operation (indicated by the red dashed line).

In order to confirm the observed SERS spectra originates from 4-MPY encapsulated in liposomes and not free 4-MPY in solution or 4-MPY bound to AuNPs, a frequency response in SERS signal was analyzed. The predicted frequency response for the zwitterionic liposomes using the theoretical CMF was verified using fluorescently tagged liposomes (data not shown). When the DEP device is operated at 1 MHz liposomes are trapped and are then repelled at 10 MHz, as compared to AuNPs which experience positive DEP over all frequencies of interest. Performing the same experiment with our platform, two devices were activated and imaged in parallel subject to the

liposome and bare AuNP spiked solution (Figure 5b). The top device was initially set at 1 MHz as a positive control (which should trap both the 70 nm liposomes and AuNPs) and the bottom device was initially set at 10 MHz (which should repel 70 nm liposomes and trap AuNPs). As expected, SERS signal was observed only on the top (1 MHz) device as compared to the bottom (10 MHz) device (Figure 5b). Then, the bottom device was switched to 1 MHz to collect both liposomes and bare AuNPs and SERS signal is observed. The SERS signal from the bottom device appears ~ 30 s after it is switched to 1 MHz and only one trapping event is detected (Figures 5b-c). The slow response is attributed to a depleted trapping volume during the initial 3 min of 10 MHz operation where liposomes were repelled and cleared from the bottom device. The trapping voltage was increased for both devices to 2 V amplitude after 1 min to extend the trapping radius of each device and an increase in SERS signal is observed from the bottom device once this occurs (Figure 5b). No increase in SERS signal is observed in the top device once it is switched to 10 MHz (Figure 5b). The liposomes already trapped at the top device are not repelled once switched to 10 MHz due to the competing AuNPs still being held by the trap. The exact same experiment was repeated using AuNPs coated in 4-MPY (Figure 5c) and SERS was observed in both the 10 and 1 MHz trapping regime, contrary to the liposome spiked with bare AuNPs solution. This frequency dependent SERS signal is indicative of its origin from liposomes and not solvated or AuNP bound 4-MPY. Our simulation and experimental results indicate that sufficient surface-enhancement for SERS from 70 nm liposome cargo can be achieved using a “sandwiched” AuNP configuration.

In conclusion, we demonstrate a rapid, dynamic, and line-multiplexed SERS device for nanovesicular studies. Our TRAIL platform can isolate 70 nm liposomes within seconds via rapid subvolt DEP and can chemically image the SERS spectra 100 times faster than a similar point-scan system. In contrast, for optically trapped individual exosomes, Raman measurements can require up to 300 s for spectra collection and currently lack multiplex imaging capabilities.⁴⁶ In addition, our lineated excitation and imaging scheme provides delay-free signal acquisition between multiplexed devices for capturing rapid dynamics in parallel. Further applications for our platform include sorting membrane-bound particles or EVs by size and/or intracellular content^{47,48} while simultaneously collecting the corresponding SERS signal. This would provide researchers the capability to rapidly isolate many nanovesicles from solution and measure a size to internal content correlation—an important factor when differentiating between microvesicles and exosomes in solution, their origin and possible means of signaling.¹⁴ While our work only utilized 70 nm gold nanoparticles, Raman enhancement may be further increased by using gold or silver nanoparticles of different sizes and shapes.⁴⁹ If chemically specific trapping is desired or trapping in conductive buffer solution, AuNPs could be functionalized to target specific receptor molecules on the nanovesicles or analytes and act as tethers for TRAIL. Metallic nanoparticles possess a positive CMF over all standard operating frequencies (1 Hz to 10 MHz) even in highly conductive buffer solutions. Our platform can also be combined with other surface-based sensing techniques such as surface plasmon resonance^{50–54} and surface-enhanced infrared absorption (SEIRA) spectroscopies.^{7,55} Furthermore, the capability to rapidly trap small particles and biomolecules

will be useful for single-cell analysis and potentially single-exosome analysis. We thus demonstrate promising results with nanogap devices in overcoming isolation and detection limits currently posed to nanovesicle research and offer a readily scalable technology to promote new avenues of dynamic SERS biosensors.

Methods. *Fabrication of High-Aspect Ratio DEP Nanogap.* The fabrication scheme for the ultralong nanogap structures via atomic layer deposition was developed and optimized in our previous work^{11,39,56} and can be classified by six key steps (Figure 1a). Initially, 500 μm thick Borofloat 33 glass wafers (University Wafer) are cleaned in a standard piranha solution and thoroughly rinsed with deionized (DI) water. A photolithography step and Au electron-evaporation deposition (150 nm Au, with a 3 nm chromium adhesion layer) is used to define the first edge of the nanogap electrode (step 1, Figure 1a). This is then followed by an atomic-layer deposition (ALD) of alumina (Al_2O_3) with variable thickness easily controlled by the user. The Al_2O_3 thickness defines the nanogaps width precisely with angstrom-scale resolution. A nominal value of 11 nm for all experiments was used (step 2, Figure 1a). After ALD, a second, nonconformal Au evaporation is performed to create the second edge of the nanogap (130 nm Au) with no adhesion layer (step 3, Figure 1a). The excess Au layer not connected to the second electrode edge is then peeled off the gap using adhesive tape (step 4, Figure 1a). Finally, using a coverslip mask, a final Au deposition creates the electrical connection to the floating electrode and a second photolithography and ion mill step is used to isolate the DEP traps (steps 5 and 6, Figure 1a). This protocol allows for DEP electrodes that are 1 mm in length and 10–20 nm wide which can be multiplexed over an entire chip. Our DEP platforms used in experiment consisted of an 800 μm wide trap to fill the field of view of our microscope for the minimum trapping voltage experiments and individual 10 μm devices to demonstrate multiplexing capabilities.

Preparation of Raman-Active and Bare Gold Nanoparticles. The 70 nm diameter citrate-stabilized AuNP (nano-Composix, 50 $\mu\text{g}/\text{mL}$) samples were diluted 1:1 with a 10 mM 4-mercaptopyridine (4-MPY) (Sigma-Aldrich) in a DI water solution for 5 min subject to sonication. The solution was then centrifuged at 7500 rpm (~ 2900 g) for 30 min. The supernatant was removed and replaced with fresh DI water. The centrifugation process was then repeated two more times. The calculated free 4-MPY in solution was 135 nM. Bare AuNP solutions were made in like-fashion. The stock solution was diluted 1:1 with DI water (rather than 10 mM 4-MPY) followed by centrifugation to remove excess citrate from solution.

Preparation of Raman-Active Phospholipid Liposomes. 1,2-Dimyristoyl-*sn*-glycero-3-phosphocholine (DMPC) and cholesterol (Avanti Polar Lipids) were mixed (4:1 molar ratio) in chloroform and dried in a vacuum desiccator overnight. The dried lipid film was then rehydrated in 5 mM 4-MPY solution at 50–60 $^\circ\text{C}$, a temperature greater than the miscibility phase transition,⁵⁷ and sonicated at this temperature for more than 2 h. The lamellarity of the vesicles was then decreased in order to improve the 4-MPY encapsulation efficiency by exposing the vesicle solution to five freeze–thaw cycles.⁵⁸ The final solution consisted of 0.5 mg/mL vesicles in DI water with 5 mM 4-MPY solution both inside and outside of the vesicles. The 70 nm liposomes were then formed using Avanti mini-extruder by sequential extrusions through 100 nm

then 50 nm polycarbonate membrane pores—a total of 21 passes each while kept at 50 °C. The mean diameter was measured to be 69.9 nm using a dynamic light scattering volume distribution measurement. Finally, free 4-MPY was removed from solution through dialysis (Slide-A-Lyzer MINI Dialysis, Thermo Scientific) using 350 μ L of solution against 1 L of DI water overnight with a total of two water changes. Before experiment, this solution was then diluted 1:1 with bare AuNPs in DI water as described above. The final solution consisted of 6 pM (12.5 μ g/mL) of bare 70 nm AuNPs and 250 μ g/mL of 70 nm liposomes encapsulating 5 mM 4-MPY solution in DI water. By using the headgroup surface area of DMPC and cholesterol and their corresponding molecular weights,⁵⁹ we could approximate the mass per liposome and molar concentration of nanovesicles. This was approximated to be 9.73 nM with an estimated 340 4-MPY molecules per liposome. The calculated free 4-MPY in solution outside of the liposomes after dialysis was calculated to be 306 pM. All liposomes were used in experiment within a day of their extrusion.

Dielectrophoretic Trapping. A sinusoidal AC signal was applied across the nanogaps with amplitudes ranging from 100 mV to 2 V. The frequency of the signals used was toggled between 1 and 10 MHz associated with positive and negative DEP for dielectric nanovesicles in DI water. This was experimentally verified using fluorescent imaging. The dielectric permittivity of the DI water solution used was $80 \times \epsilon_0$, and the conductivity was measured to be approximately 4×10^{-4} S/m (measured by B-771 LAQUATwin, Horiba Scientific). The dielectric permittivity and conductivity values for the liposome membrane and inner-liposome solution were taken from Biasio et al. in which the zwitterionic properties were assumed.⁴⁵ These reported effective values for 70 nm liposomes were measured for the membrane to be $25 \times \epsilon_0$ and 10^{-5} S/m and for the inner liposome solution to be $80 \times \epsilon_0$ and 4×10^{-2} S/m. The thickness of the liposome membrane was approximated to be 5 nm, and a simple single shell model was used to model the DEP trapping properties. Trapping volumes were approximated using the same approach as described in our previous work.¹¹

Line-Raman Spectroscopy. A Nikon Eclipse Ti microscope was used to image and collect in the epi-configuration with all images taken in the bright-field mode. The output of an OBIS LX 785, 100 mW diode laser (Coherent) was first passed through a short-pass filter (800 nm cutoff, Thorlabs) and converted to a laser-line using a Powell lens (L_1 , fan angle 30°, Thorlabs) and two orthogonally oriented cylindrical lens (L_2 and L_3 , f.l. 13.7 and 80 mm, Thorlabs) (Figure 1b). This created an image of a laser-line at P_1 (Figure 1b). A spherical plano-convex lens (L_4 , f.l. 400 mm, Thorlabs) was then used to take the Fourier transform of the line at P_2 before being reimaged by the microscope objective (L_5 , 100 \times , NA 1.25, oil immersion, Nikon) (Figure 1b). A 785 RazorEdge long-pass dichroic mirror (Semrock) was used to reflect the laser-line illumination to the sample and pass the Stokes-shifted SERS spectra for collection. A tube lens imaged the sample at the side port of the microscope. This was then passed through another spherical plano-convex lens (f.l. 200 mm, Thorlabs) and then the rest of the excitation source was filtered using a 785 nm notch filter (Thorlabs). Finally, the sample was reimaged by a spherical plano-convex lens (f.l. 200 mm, Thorlabs) at the slit of an imaging spectrometer (SpectraPro sp2300, Princeton Instruments) and recorded by a CCD

camera (Pixis 400, Princeton Instruments). The CCD camera consisted of a 1338×400 pixel array with the measured projected pixel size onto the sample to be 194 nm². During SERS measurements, 1D imaging was made along the 400 pixel dimension while the corresponding spectrum was collected along the 1338 pixel dimension, with no binning of the pixels in either direction. The dimensions of the line were characterized to be 40 μ m \times 800 nm. The average width of the line profile (along the short direction) was fit to a Gaussian using MATLAB where the full-width half-max of this Gaussian was found to be 800 nm using the most conservative tolerance parameters. Likewise, the profile along the long direction was plotted and found that the edge lobes maintained 1.5–2 times more radiation than the center of the line. Data collection was kept to the center of the line where the profile was more uniform. A power meter (Thorlabs) was used to measure the laser-line power directly after the objective. An image of the line was taken with a dark image removed (Figure 1d). The counts were then integrated across the entire image and set equal to the measured power from the meter. Assuming a linear relationship between counts and laser-power, the power-density image (Figure 1d) could then be mapped. The peak power density measured was 425.6 μ W/ μ m² (Figure 1d). All data was managed using LightView software (Princeton Instruments) and analyzed using a custom MATLAB script. The SERS background spectra were removed using a spline interpolation function. Any small linear shifts in the grating of the spectrometer between experiments were accounted for using a least-squares solution to calibrate linear shifts between the SERS peaks and their expected values.⁴²

■ ASSOCIATED CONTENT

📄 Supporting Information

The Supporting Information is available free of charge on the ACS Publications website at DOI: 10.1021/acs.nanolett.8b02654.

Simulations of 200 different AuNP configurations with the nanogap combined enhancement factor, negative control–liposome SERS carrying 4-MPY with no AuNPs, and peak variability (PDF)

■ AUTHOR INFORMATION

Corresponding Author

*(S.-H.O.) E-mail: sang@umn.edu.

ORCID

Nathan J. Wittenberg: 0000-0001-9196-1867

Wei-Chuan Shih: 0000-0002-7530-7352

Sang-Hyun Oh: 0000-0002-6992-5007

Notes

The authors declare no competing financial interest.

■ ACKNOWLEDGMENTS

This work was supported by grants from the National Science Foundation (NSF ECCS Grant No. 1610333 to C.T.E. and S.-H.O.; NSF CBET Grant No. 1605683 to W.-C.S.) and the Minnesota Partnership for Biotechnology and Medical Genomics (A.B., N.J.W., and S.-H.O.). C.T.E. and D.J.K. acknowledge support from the NSF Graduate Research Fellowship Program (GRFP) and A.B. acknowledges support from the University of Minnesota Doctoral Dissertation Fellowship. N.J.W. acknowledges support from Lehigh

University. Device fabrication was performed at the University of Minnesota Nanofabrication Center, which receives support from the NSF through the National Nanotechnology Coordinated Infrastructure (NNCI) program.

REFERENCES

- (1) Xu, H.; Bjerneld, E.; Käll, M.; Borjesson, L. *Phys. Rev. Lett.* **1999**, *83*, 4357–4360.
- (2) Ward, D. R.; Grady, N. K.; Levin, C. S.; Halas, N. J.; Wu, Y.; Nordlander, P.; Natelson, D. *Nano Lett.* **2007**, *7*, 1396–1400.
- (3) Halas, N. J.; Lal, S.; Chang, W.-S.; Link, S.; Nordlander, P. *Chem. Rev.* **2011**, *111*, 3913–3961.
- (4) Lim, D.-K.; Jeon, K.-S.; Hwang, J.-H.; Kim, H.; Kwon, S.; Suh, Y. D.; Nam, J.-M. *Nat. Nanotechnol.* **2011**, *6*, 452–460.
- (5) Huck, C.; Neubrech, F.; Vogt, J.; Toma, A.; Gerbert, D.; Katzmann, J.; Härtling, T.; Pucci, A. *ACS Nano* **2014**, *8*, 4908–4914.
- (6) Chen, X.; Ciraci, C.; Smith, D. R.; Oh, S.-H. *Nano Lett.* **2015**, *15*, 107–113.
- (7) Dong, L.; Yang, X.; Zhang, C.; Cerjan, B.; Zhou, L.; Tseng, M. L.; Zhang, Y.; Alabastri, A.; Nordlander, P.; Halas, N. J. *Nano Lett.* **2017**, *17*, 5768–5774.
- (8) Xu, H.; Käll, M. *Phys. Rev. Lett.* **2002**, *89*, 246802.
- (9) Pang, Y.; Gordon, R. *Nano Lett.* **2012**, *12*, 402–406.
- (10) Yoo, D.; Gurunatha, K. L.; Choi, H.-K.; Mohr, D. A.; Ertsgaard, C. T.; Gordon, R.; Oh, S.-H. *Nano Lett.* **2018**, *18*, 3637–3642.
- (11) Barik, A.; Chen, X.; Oh, S.-H. *Nano Lett.* **2016**, *16*, 6317–6324.
- (12) Raposo, G.; Stoorvogel, W. *J. Cell Biol.* **2013**, *200*, 373–383.
- (13) Boriachek, K.; Islam, M. N.; Möller, A.; Salomon, C.; Nguyen, N. T.; Hossain, M. S. A.; Yamauchi, Y.; Shiddiky, M. J. A. *Small* **2018**, *14*, 1702153.
- (14) Vlassov, A. V.; Magdaleno, S.; Setterquist, R.; Conrad, R. *Biochim. Biophys. Acta, Gen. Subj.* **2012**, *1820*, 940–948.
- (15) Melo, S. A.; Luecke, L. B.; Kahlert, C.; Fernandez, A. F.; Gammon, S. T.; Kaye, J.; LeBleu, V. S.; Mittendorf, E. A.; Weitz, J.; Rahbari, N.; Reissfelder, C.; Pilarsky, C.; Fraga, M. F.; Piwnicka-Worms, D.; Kalluri, R. *Nature* **2015**, *523*, 177–182.
- (16) Cho, H.; Lee, B.; Liu, G. L.; Agarwal, A.; Lee, L. P. *Lab Chip* **2009**, *9*, 3360–3363.
- (17) Yanik, A. A.; Huang, M.; Kamohara, O.; Artar, A.; Geisbert, T. W.; Connor, J. H.; Altug, H. *Nano Lett.* **2010**, *10*, 4962–4969.
- (18) Jonsson, M. P.; Dahlin, A. B.; Feuz, L.; Petronis, S.; Höök, F. *Anal. Chem.* **2010**, *82*, 2087–2094.
- (19) Escobedo, C.; Brolo, A. G.; Gordon, R.; Sinton, D. *Nano Lett.* **2012**, *12*, 1592–1596.
- (20) De Angelis, F.; Gentile, F.; Mearini, F.; Das, G.; Moretti, M.; Candeloro, P.; Coluccio, M. L.; Cojoc, G.; Accardo, A.; Liberale, C.; Zaccaria, R. P.; Perozziello, G.; Tirinato, L.; Toma, A.; Cuda, G.; Cingolani, R.; Di Fabrizio, E. *Nat. Photonics* **2011**, *5*, 682–687.
- (21) Tantussi, F.; Messina, G. C.; Capozza, R.; Dipalo, M.; Lovato, L.; De Angelis, F. *ACS Nano* **2018**, *12*, 4116–4122.
- (22) Pohl, H. A. *Dielectrophoresis: the behavior of neutral matter in nonuniform electric fields*; Cambridge Univ Press: 1978.
- (23) Becker, F. F.; Wang, X.-B.; Huang, Y.; Pethig, R.; Vykoukal, J. V.; Gascoyne, P. R. C. *Proc. Natl. Acad. Sci. U. S. A.* **1995**, *92*, 860–864.
- (24) Hu, X.; Bessette, P.; Qian, J.; Meinhart, C.; Daugherty, P. S.; Soh, H. T. *Proc. Natl. Acad. Sci. U. S. A.* **2005**, *102*, 15757–15761.
- (25) Froude, V. E.; Zhu, Y. *J. Phys. Chem. B* **2009**, *113*, 1552–1558.
- (26) Shi, L.; Rana, A.; Esfandiari, L. *Sci. Rep.* **2018**, *8*, 6751.
- (27) Tuukkanen, Toppari, Kuzyk; Hirviniemi; Hytönen; Ihalainen, A.; Törmä. *Nano Lett.* **2006**, *6*, 1339–1343.
- (28) Lesser-Rojas, L.; Ebbinghaus, P.; Vasan, G.; Chu, M.-L.; Erbe, A.; Chou, C.-F. *Nano Lett.* **2014**, *14*, 2242–2250.
- (29) Barik, A.; Zhang, Y.; Grassi, R.; Nadappuram, B. P.; Edel, J. B.; Low, T.; Koester, S. J.; Oh, S.-H. *Nat. Commun.* **2017**, *8*, 1867.
- (30) Kundu, J.; Levin, C. S.; Halas, N. J. *Nanoscale* **2009**, *1*, 114–117.
- (31) Ertsgaard, C. T.; McKoskey, R. M.; Rich, I. S.; Lindquist, N. C. *ACS Nano* **2014**, *8*, 10941–10946.
- (32) Bantz, K. C.; Meyer, A. F.; Wittenberg, N. J.; Im, H.; Kurtuluş, Ö.; Lee, S. H.; Lindquist, N. C.; Oh, S.-H.; Haynes, C. L. *Phys. Chem. Chem. Phys.* **2011**, *13*, 11551–11567.
- (33) Talley, C. E.; Jackson, J. B.; Oubre, C.; Grady, N. K.; Hollars, C. W.; Lane, S. M.; Huser, T. R.; Nordlander, P.; Halas, N. J. *Nano Lett.* **2005**, *5*, 1569–1574.
- (34) Haynes, C. L.; McFarland, A.; Van Duyne, R. P. *Anal. Chem.* **2005**, *77*, 338A–346A.
- (35) Lum, W.; Bruzas, I.; Gorunmez, Z.; Unser, S.; Beck, T.; Sagle, L. *J. Phys. Chem. Lett.* **2017**, *8*, 2639–2646.
- (36) Qi, J.; Shih, W.-C. *Appl. Opt.* **2014**, *53*, 2881–2885.
- (37) Squires, T. M. *Lab Chip* **2009**, *9*, 2477–2483.
- (38) Miyazaki, H. T.; Kurokawa, Y. *Phys. Rev. Lett.* **2006**, *96*, 097401.
- (39) Im, H.; Bantz, K. C.; Lindquist, N. C.; Haynes, C. L.; Oh, S.-H. *Nano Lett.* **2010**, *10*, 2231–2236.
- (40) Sudheendran, N.; Qi, J.; Young, E. D.; Lazar, A. J.; Lev, D. C.; Pollock, R. E.; Larin, K. V.; Shih, W.-C. *Laser Phys. Lett.* **2014**, *11*, 105602.
- (41) Qiu, S.; Zhao, F.; Zenasni, O.; Li, J.; Shih, W.-C. *ACS Appl. Mater. Interfaces* **2016**, *8*, 29968–29976.
- (42) Hu, J.; Zhao, B.; Xu, W.; Li, B.; Fan, Y. *Spectrochim. Acta, Part A* **2002**, *58*, 2827–2834.
- (43) Lee, S. H.; Lindquist, N. C.; Wittenberg, N. J.; Jordan, L. R.; Oh, S.-H. *Lab Chip* **2012**, *12*, 3882–3890.
- (44) Keller, C.; Kasemo, B. *Biophys. J.* **1998**, *75*, 1397–1402.
- (45) Di Biasio, A.; Cametti, C. *Bioelectrochemistry* **2007**, *70*, 328–334.
- (46) Smith, Z. J.; Lee, C.; Rojalin, T.; Carney, R. P.; Hazari, S.; Knudson, A.; Lam, K.; Saari, H.; Ibañez, E. L.; Viitala, T.; Laaksonen, T.; Yliperttula, M.; Wachsmann-Hogiu, S. *J. Extracell. Vesicles* **2015**, *4*, 28533.
- (47) Block, S.; Fast, B. J.; Lundgren, A.; Zhdanov, V. P.; Höök, F. *Nat. Commun.* **2016**, *7*, 12956.
- (48) Friedrich, R.; Block, S.; Alizadehheidari, M.; Heider, S.; Fritzsche, J.; Esbjörner, E. K.; Westerlund, F.; Bally, M. *Lab Chip* **2017**, *17*, 830–841.
- (49) Lal, S.; Link, S.; Halas, N. J. *Nat. Photonics* **2007**, *1*, 641–648.
- (50) Brolo, A. G.; Gordon, R.; Leathem, B.; Kavanagh, K. L. *Langmuir* **2004**, *20*, 4813–4815.
- (51) Dahlin, A. B.; Zäch, M.; Rindzevicius, T.; Käll, M.; Sutherland, D. S.; Höök, F. *J. Am. Chem. Soc.* **2005**, *127*, 5043–5048.
- (52) Im, H.; Lee, S. H.; Wittenberg, N. J.; Johnson, T. W.; Lindquist, N. C.; Nagpal, P.; Norris, D. J.; Oh, S.-H. *ACS Nano* **2011**, *5*, 6244–6253.
- (53) Wittenberg, N. J.; Im, H.; Johnson, T. W.; Xu, X.; Warrington, A. E.; Rodriguez, M.; Oh, S.-H. *ACS Nano* **2011**, *5*, 7555–7564.
- (54) Jackman, J. A.; Rahim Ferhan, A.; Cho, N.-J. *Chem. Soc. Rev.* **2017**, *46*, 3615–3660.
- (55) Limaj, O.; Etezadi, D.; Wittenberg, N. J.; Rodrigo, D.; Yoo, D.; Oh, S.-H.; Altug, H. *Nano Lett.* **2016**, *16*, 1502–1508.
- (56) Chen, X.; Park, H.-R.; Pelton, M.; Piao, X.; Lindquist, N. C.; Im, H.; Kim, Y. J.; Ahn, J. S.; Ahn, K. J.; Park, N.; Kim, D.-S.; Oh, S.-H. *Nat. Commun.* **2013**, *4*, 2361.
- (57) Almeida, P. F. F.; Vaz, W. L. C.; Thompson, T. E. *Biochemistry* **1992**, *31*, 6739–6747.
- (58) Mayer, L. D.; Hope, M. J.; Cullis, P. R.; Janoff, A. S. *Biochim. Biophys. Acta, Biomembr.* **1985**, *817*, 193–196.
- (59) Israelachvili, J. N.; Mitchell, D. J. *Biochim. Biophys. Acta, Biomembr.* **1975**, *389*, 13–19.